ADVANCED MATERIALS
www.advmat.de

Contactless User-Interactive Sensing Display for Human–Human and Human–Machine Interactions

Jiaqi He, Ruilai Wei, Xiaole Ma, Wenqiang Wu, Xiaojun Pan, Junlu Sun, Jiaqi Tang, Zhangsheng Xu, Chunfeng Wang, and Caofeng Pan**

Creating a large-scale contactless user-interactive sensing display (CUISD) with optimal features is challenging but crucial for efficient human–human or human–machine interactions. This study reports a CUISD based on dynamic alternating current electroluminescence (ACEL) that responds to humidity. Subsecond humidity-induced luminescence is achieved by integrating a highly responsive hydrogel into the ACEL layer. The patterned silver nanofiber electrode and luminescence layer, produced through electrospinning and microfabrication, result in a stretchable, large-scale, high-resolution, multicolor, and dynamic CUISD. The CUISD is implemented for the real-time control of a remote-controlled car, wherein the luminescence signals induced by touchless finger movements are distinguished and encoded to deliver specific commands. Moreover, the distinctive recognition of breathing facilitates the CUISD to serve as a visual signal transmitter for information interaction, which is particularly beneficial for individuals with disabilities. The paradigm shift depicts in this work is expected to reshape the way authors interact with each other and devices, discovering niche applications in virtual/augmented reality and the metaverse.

1. Introduction

The emergence of artificial intelligence and metaverse technology has boosted the revolution of human–machine interactions from rigid buttons and panels to soft interface electronics with unprecedented performances.[1–5] User-interactive sensing displays (UISDs) can sense and convert human stimuli into human-readable visual signals, thereby enhancing the operability and dexterity of human–machine interactions through hand–eye coordination and offering significant convenience for nondigital users.[6–8] Consequently, different UISDs have been developed by embedding pressure-sensing elements into electroluminescent/electrochromic devices,[9–13] developing metasurfaces with reconfigurable structural colors,[14,15] and utilizing novel mechanochromic/mechanoluminescent materials.[16–21] However, these UISDs are generally pressure-sensing or strain-sensing devices, where physical contact is required for sensing and display. Such direct physical contact not only confines the interactive motions to simple touching or sliding but also imposes serious restrictions on remote or hygiene-focused sensing applications. Additionally, frequent physical contact results in inevitable mechanical wear and fatigue, shortening the device's lifespan. Hence, the development of revolutionary contactless user-interactive sensing displays (CUISDs) that facilitate versatile, convenient, hygienic, and long-lasting interaction is in high demand, especially for individuals with disabilities.

Recent studies have revealed interesting progress in contactless sensors for user-interactive interfaces by recognizing changes in capacitance,[22,23] humidity,[24] magnetic field,[25,26] thermal radiation,[27,28] and electrostatic induction.[29–31] For example, Liu et al. demonstrated a triboelectric sensor that could perform simultaneous tactile and touchless sensing, permitting touchless interactive teaching of soft robots to perform skilled locomotion.[32] Kamijo et al. reported a near-infrared-sensitive organic photodetector array that can detect near-infrared light reflected from the fingers and hands, enabling touchless gesture recognition and control.[33] However, these sensors capture information and transfer it into electrical signals; thus they cannot provide real-time visual feedback to the user owning to the absence of a light medium. To addressing this issue, the sensor is linked to a display via a microcontroller.

J. He, R. Wei, X. Ma, W. Wu, X. Pan, J. Sun, J. Tang, Z. Xu, C. Pan
Beijing Institute of Nanoenergy and Nanosystems
Chinese Academy of Sciences
Beijing 101400, China
E-mail: pancaofeng@buaa.edu.cn
J. He, C. Pan
Institute of Atomic Manufacturing
Beihang University
Beijing 100191, China
The ORCID identification number(s) for the author(s) of this article can be found under https://doi.org/10.1002/adma.202401931
J. He, J. Tang, Z. Xu, C. Pan
School of Nanoscience and Engineering
University of Chinese Academy of Sciences
Beijing 100049, China
C. Wang
Guangdong Research Center for Interfacial Engineering of Functional Materials
College of Materials Science and Engineering
Shenzhen University
Shenzhen 518060, China
E-mail: cfwang@szu.edu.cn

DOI: 10.1002/adma.202401931

However, the serial connection among the three components is intricate and requires an energy-lossy interconnection circuit, resulting in a cumbersome and energy-inefficient interaction system. How to combine contactless sensors with luminescence technology in an efficient and elegant manner to construct a single-device CUISD presents a significant challenge. Several impressive studies have recently shown the feasibility by developing magneto-interactive electroluminescence[34] or humidity-/infrared radiation-responsive structural color;[35,36] however, the former requires an additional magnetic object during operation, whereas the latter suffers from insufficient color rendering and mechanical compliance. Furthermore, ensuring optimal user experience imposes additional demands on the CUISD: i) stretchability and ease of fabrication to enable large-scale wearable applications; ii) fast and stable sensing of noncontact stimuli; iii) multicolor, dynamic and high-spatial-resolution display of the sensing signals; and iv) easily identifiable signals for contactless human–human or human–machine interaction.

Herein, we present a single-device CUISD to address all the aforementioned requirements. The CUISD has a hierarchical architecture composed of a humidity-sensing hydrogel layer on top, alternating current electroluminescence (ACEL) layer in the middle, and interdigitated multilayer silver nanofiber (Ag NF) electrodes at the bottom. The conductivity changes of the hydrogel as a fingertip approaches or from a human breath trigger the subsecond dynamic response of the ACEL, facilitating noncontact sensing and display. The use of optimized multilayered Ag NF electrode contributes to the large-scale fabrication of CUISD with good stretchability and robustness. The patterned ACEL layer enables multicolor and dynamic visualization of humidity changes at a high spatial resolution. By exploiting the ability of the CUISD to visualize finger proximity and track its position, real-time control of a remote-controlled (RC) car by contactless finger movement was demonstrated. Moreover, we designed a breath-based smart mask for visual human–human and human–machine interactions by encoding luminescent signals into Morse or binary code, providing an alternative interactive route for users with impaired movement or occupied hands.

2. Results and Discussion

2.1. Design and Working Mechanism of the CUISD

The schematic structure of the CUISD is depicted in **Figure 1a**, showcasing a stretchable large-area CUISD with pixels connected in parallel through an interdigitated Ag NF electrode. Each pixel can light up in response to the humidity of the fingertip. The magnified view (Figure 1b) of one representative pixel reveals that there is five main layers arranging from top to bottom: the sensing layer, luminescence layer, dielectric layer, electrode layer, and substrate. The sensing layer comprises a humidity-sensitive hygroscopic hydrogel. The luminescent layer consists of a mixture of polydimethylsiloxane (PDMS) and ACEL particles. The dielectric layer is formed by combining $BaTiO_3$ (BTO) nanoparticles with PDMS. The electrode layer, depicted in Figure 1c, consists of multilayered hollow Ag NFs embedded in the PDMS substrate, featuring excellent tensile conductivity and transparency. Figure 1d presents photographs of the CUISD under different conditions. The device remained nonluminescent after the power was turned on under a relative humidity (RH) of 20%, as shown in Figure 1d-i. In contrast, at a high RH (≈80%), the device exhibited bright electroluminescence on both the front (Figure 1d-ii) and backside (Figure 1d-iii). Furthermore, as shown in Figure 1d-iv, the device luminesces when the fingertip approaches under a low RH, demonstrating its excellent noncontact interactive display capability. The working mechanism enabling humidity-sensitive luminescence was analyzed from the cross-section of the device, as illustrated in Figure 1e. Under low-humidity conditions, the electric field is insufficient for stimulating the ACEL particles for electroluminescence owning to the wide gap between electrodes and poor conductivity of the sensing layer. Conversely, under high-humidity conditions, the sensing layer features an enhanced conductivity due to more absorbed water molecules. This causes the electric field between the electrodes and the sensing layer to surpass the threshold of $\approx 10^6$ V m^{-1} (see the simulation of the electric field strength distribution of the luminescence layer in Figure S1, Supporting Information), inducing electroluminescence in the luminescence layer.

2.2. Multilayered Ag NF Electrode for the CUISD

The development of stretchable and transparent electrodes is the first step toward achieving high-performance intrinsically stretchable CUISD. Inspired by the naturally high transparency and excellent tensile properties of silk, a multilayered Ag NF electrode with a 2D ramified structure was prepared via a combination of electrostatic spinning, magnetron sputtering, photolithography, wet etching, and transfer printing. The schematic of the fabrication process is shown in Figure S2 (Supporting Information) and detailed fabrication parameters are provided in the Experimental Section. Intricate electrode patterns with defined features were achieved, as shown in **Figure 2a**. The linewidth can be reduced to several tens of micrometers, and sharp and clear edges were obtained, indicating the high patterning accuracy of the electrode.

The number of the Ag NF layers greatly affects the stretchability, conductivity, and transparency of the electrode. Therefore, electrodes with different numbers of Ag NF layers were prepared and investigated. As shown in Figure 2b, the areal density of the Ag NF gradually increased with the number of layers, which were connected to each other via longitudinal lapping, thereby increasing the conductive pathways. After being transferred from the glass to the PDMS substrate, the Ag NFs were embedded into the PDMS with a small number of exposed Ag NFs on the surface to ensure charge transfer, which is indicated by the conductive atomic force microscopy (C-AFM) image and scanning electron microscopy (SEM) image, as shown in Figures 2c and S3 (Supporting Information), respectively. The encapsulation of Ag NFs not only improved the average surface roughness (Ra) of the electrode from 321.92 to 20.21 nm (Figure 2d), enabling the seamless connection between the electrodes and others but also endowed the robustness of the electrode, which can be reversibly deformed in various modes (Figure 2e). The diameters of the Ag NFs were in the range of 300–700 nm, as shown in Figure 2f. Figure 2g shows the relative resistance changes ($\Delta R/R_0$) of the Ag NF electrodes with different numbers of layers during

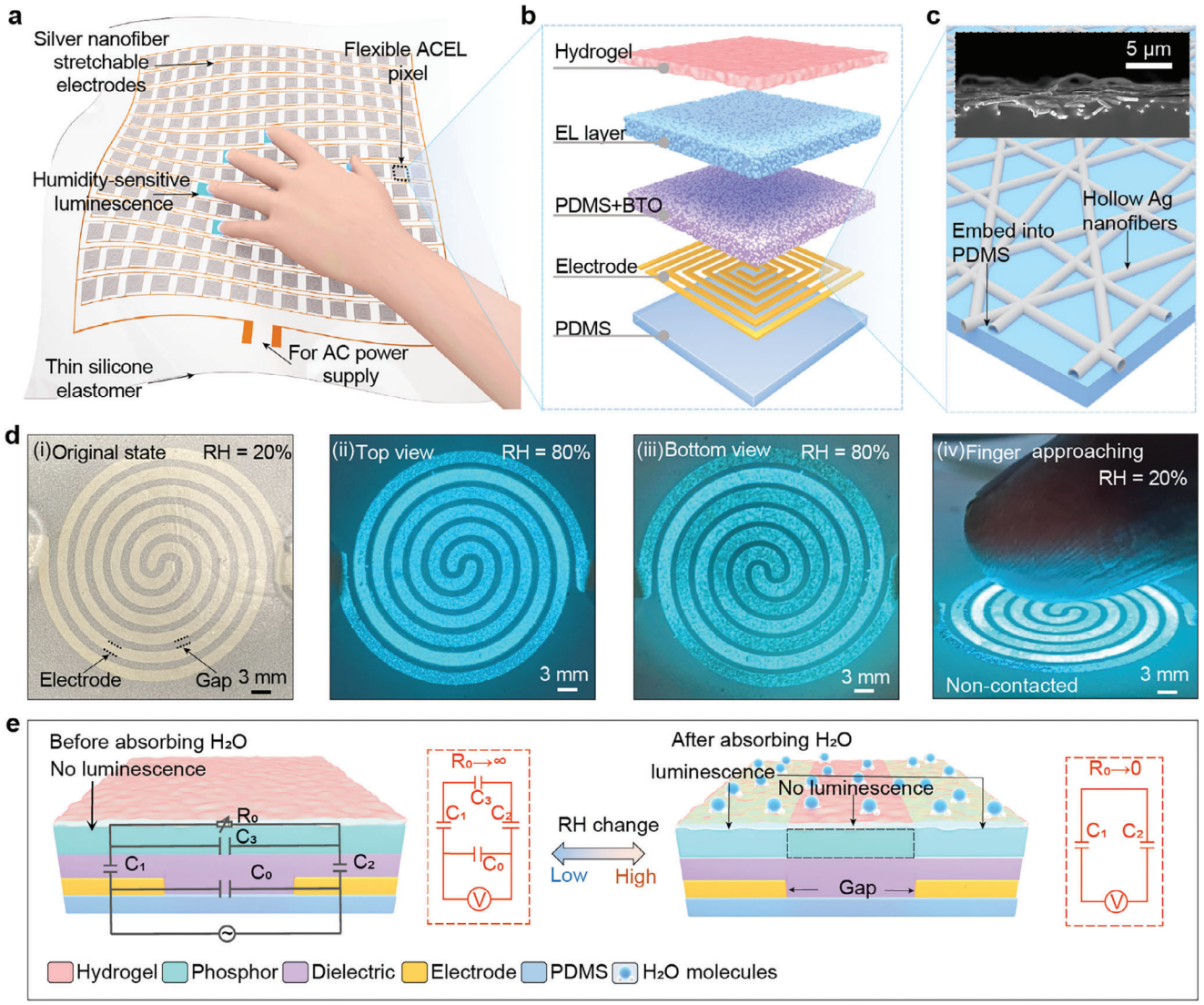

Figure 1. Design and working mechanism of the CUISD. a) Schematic of the stretchable large-area CUISD. b) Exploded view of an individual pixel of the CUISD. c) Schematic and SEM images of the hollow Ag NFs embedded in PDMS. d-i) Photograph of the CUISD at the RH of 20% after the power was turned on. d-ii) Top view of the CUISD at 80% RH after the power was turned on. d-iii) The bottom view of the CUISD at 80% RH after the power was turned on. d-iv) Photograph of the CUISD responding to fingertip proximity at 20% RH after the power was turned on. e) Schematic of the working mechanism of the CUISD.

stretching. As the number of layers was increased, $\Delta R/R_0$ decreased, resulting from the increased connecting channels among the Ag NFs. In addition, the square resistance of the electrode surface decreased as the number of layers increased owing to the increase in the electrode thickness, leading to more connection sites between the Ag NFs (Figure 2h). Although the increase in the number of layers improved the electrical conductivity, it can also cause several problems. In particular, the increase in the number of electrode layers complicates the preparation process. Moreover, it increases the areal density of the Ag NFs, thereby decreasing the transparency from 90% to 60%, as shown in Figure 2i. Consequently, we selected a three-layer Ag NF electrode for the device fabrication, which exhibited a stable electrical performance under bending and twisting (Figure 2j,k) and low resistance of <20 Ω for over 5000 stretching cycles (Figure 2l) and <100 Ω for 15 000 stretching cycles (inset of Figure 2l) at a 50% strain, confirming its reliability.

2.3. Fabrication and Characterizations of the CUISD

Figure 3a illustrates the architecture of a CUISD pixel, in which the electrode comprised three layers of Ag NFs embedded in PDMS, as previously described. The hierarchical structure of the hydrogel/ZnS: Cu/BTO/Ag NFs/PDMS can be clearly identified in the cross-sectional SEM and energy-dispersive spectroscopy (EDS) maps, as shown in Figure 3b,c, respectively. For the ACEL device, a dielectric layer with a high dielectric constant can focus the electric field on the emissive layer and lower the external driving voltage required to generate light. Thus, the dielectric

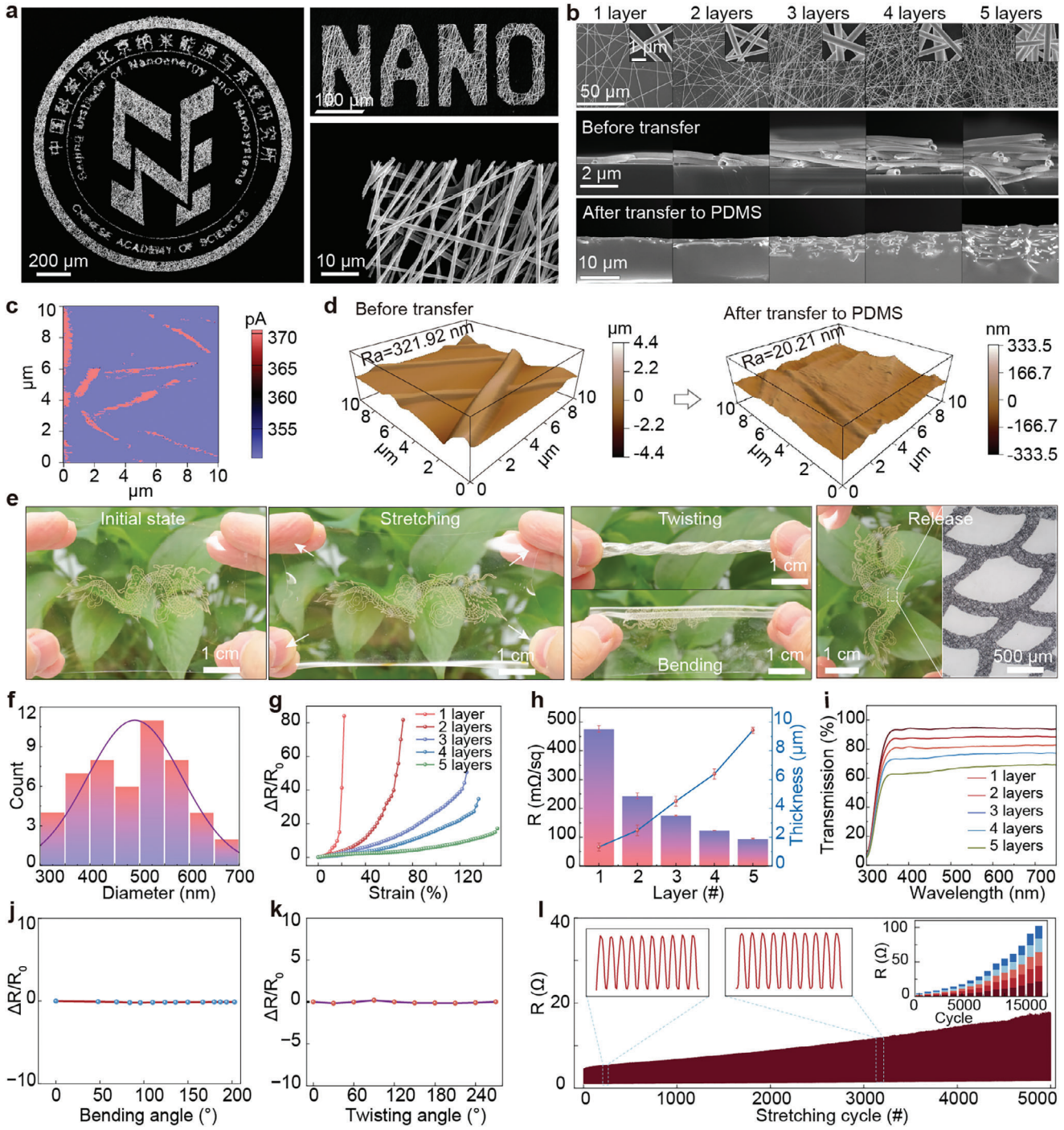

Figure 2. Multilayered Ag NF electrode for the CUISD. a) SEM images of the patterned Ag NF electrode. b) SEM images of the Ag NF electrode with different numbers of Ag NF layers. c) The C-AFM image of the Ag NFs after being transferred from the glass to the PDMS substrate. d) AFM images of the Ag NFs before and after embedding in PDMS. e) Optical images of the Ag NF electrode upon different deformations, showing its mechanical compliance and transparency. f) Diameter distribution of the Ag NFs. g) The relative resistance changes ($\Delta R/R_0$) of the Ag NF electrodes with different numbers of layers during stretching. h) Thickness and square resistance of the Ag NF electrodes with different numbers of layers. The error bars were based on the standard deviation results of independent measurements of the three devices. i) Transmission spectra of the Ag NF electrodes with different numbers of layers. j,k) $\Delta R/R_0$ of a three-layer Ag NF electrode under bending or twisting at different angles, respectively. l) Stability of a three-layer Ag NF electrode under different stretching cycles.

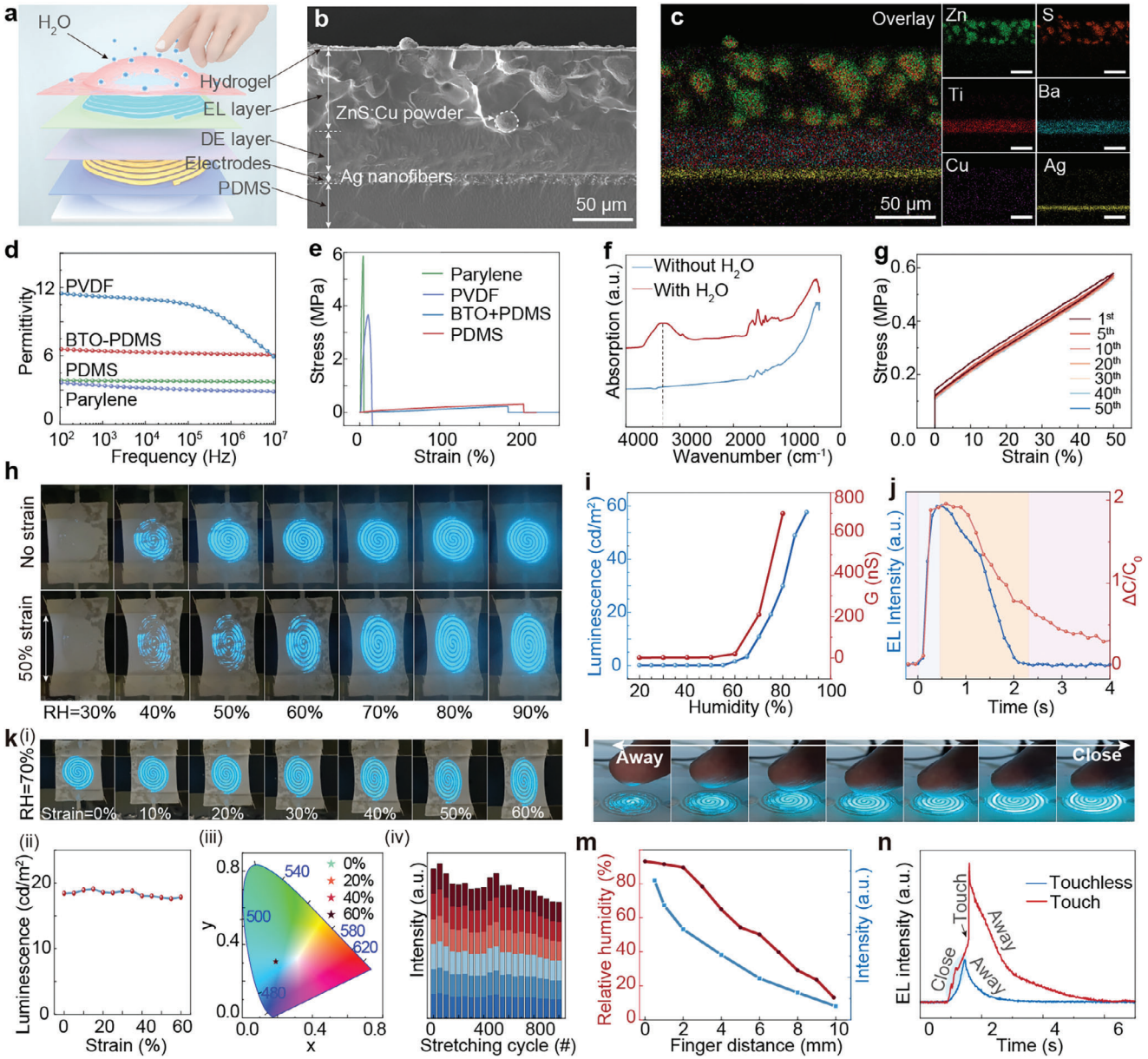

Figure 3. Fabrication and characterizations of the CUISD. a) Schematic of a CUISD pixel. b,c) Cross-section SEM image and EDS mapping images of the CUISD, respectively. d) Permittivity of different dielectric materials. e) Stress–strain curves of different dielectric materials. f) Fourier transform infrared spectra of the hydrogel sensing layer before and after the absorption of water molecules. g) Stress–strain curves of the CUISD device under cyclic stretching. h) Optical images of the CUISD under different RH levels at a strain of 0% and 50%. i) Luminescence intensity and conductivity of the CUISD under different RH. j) Response times of the CUISD to rapid humidity changes. k) Luminescence of the CUISD device under different applied strains at 70% RH. l,m) Response behaviors of the CUISD device to the approach of a fingertip. n) Luminescence intensity of the CUISD with the finger approach and contact.

layer of the BTO particles embedded in PDMS (BTO-PDMS) was selected considering a tradeoff between the permittivity and the stretchability. As shown in Figure 3d, the frequency-dependent dielectric constant of BTO-PDMS is higher than that of pure PDMS and parylene but lower than that of a polyvinylidene fluoride (PVDF) film. However, the tensile fracture strain of PVDF was only 5%, which is considerably smaller than that of BTO-PDMS (up to 180%), as indicated in the stress–strain curves in Figure 3e. The good stretchability of BTO-PDMS benefits from the homogeneous dispersion of BTO particles in PDMS owning to the surface treatment of the BTO particles (Figure S4, Supporting Information). Figure 3f shows the infrared spectra of the hygroscopic hydrogel in response to moisture, in which an obvious peak at 3500–3800 cm^{-1} can be observed after absorbing water molecules, indicating the good humidity sensitivity of the hydrogel. The results of the cyclic stretching tests of the CUISD device are shown in Figure 3g, showing a hysteresis loop in the first cycle owning to the initial energy dissipation and a good overlap

between the second and the 50th cycles, indicating the excellent mechanical stability of the device within an elastic strain of 50%.

The luminescence response of the CUISD to humidity under an AC power supply (110 V, 2 kHz) was explored. As shown in Figure 3h, the luminescent imagery of the CUISD at varying humidity levels illustrates a clear increase in the luminescent area and brightness as RH increased from 30% to 90%. Even under a tensile strain of 50%, the CUISD consistently exhibited stable humidity-induced luminescence. Figure 3i shows the positive correlation between the luminescence intensity of CUISD and RH. This correlation is ascribed to the increase in the conductivity of the sensing layer due to the elevated humidity. For contactless sensors, response speed is an important factor for practical applications. The response times of the CUISD to rapid humidity changes are depicted in Figure 3j. The CUISD exhibited subsecond responses (0.4 s for luminescence intensity and 0.5 s for capacitance) to humidity fluctuations from 30% to 90% and prompt disappearance of luminescence within 2 s as the RH was reverted to 30%. Luminescent stability is a critical property for displays, especially stretchable ones. As shown in Figure 3k-i and Video S1 (Supporting Information), the CUISD maintained stable luminescence at 70% RH despite increasing applied strain. The brightness was maintained in the range of 17–19 cd m^{-2} (Figure 3k-ii). Stability during stretching is attributed to the opposing effects of thinning and widening, which counteract electric-field changes. The chromaticity diagram demonstrates that stretching did not alter the luminescence of the device (Figure 3k-iii). After 1000 cycles of stretching at 50% strain and 70% RH, the luminescence intensity of the CUISD decreased by less than 20%, attesting to its excellent luminescence stability and tensile durability. By utilizing the natural humidity of the human skin, CUISD can respond to the approach of a fingertip. As shown in Figure 3l,m, the luminescence intensity and area gradually increased as the fingertip approached owing to the distance-dependent humidity field surrounding the fingertip. The CUISD maintained its humidity responsiveness even under the strain of the finger joint (Figure S5, Supporting Information). Moreover, direct fingertip contact can induce enhanced luminescence because it enables higher moisture adsorption on the CUISD surface. Consequently, the CUISD opens up possibilities for displaying handwritten letters or trajectory monitoring of mollusks, and the differentiation between contact and noncontact humidity sensing can be also realized, as shown in Figures 3n and S6 (Supporting Information).

2.4. Large-Scale, High-Resolution, and Multicolor CUISD for Dynamic Display and Motion Tracking

Dynamic display can alter patterns in response to interactive signals, enhancing the user experience with an intuitive visual impact. Through a comprehensive exploration of the working mechanism of ACEL, we devised a CUISD capable of achieving dynamic pattern changes triggered by humidity. As previously mentioned, CUISD remains nonluminescent at a low RH owning to the weak electric fields, resulting from the wide gap (>350 µm) between the electrodes and the poor conductivity of the sensing layer. When the electrode gap width was decreased (<350 µm), CUISD triggered inter-gap electroluminescence at a low RH by intensifying the electric field between the electrodes, as illustrated in the left panel **Figure** 4a. However, at high RH, luminescence occurred between the electrodes and the sensing layer, where the electric field was enhanced by water absorption. Simultaneously, the electric field at the gap weakened, causing the luminescence there to vanish, as illustrated in the right panel of Figure 4a. Thus, the humidity modulation can facilitate a dynamic transition between luminescence at the gaps and that at the electrodes. Combined with the patterned deposition of luminescent pixels via microfabrication (see Experimental Section for details), the dynamic display of an expression was demonstrated. As shown in Figure 4b and Video S2 (Supporting Information), the CUISD displayed a crying expression at low RH and then transferred to a laughing expression as RH increased. Furthermore, a dynamic display with additional color changes can be realized using different ACEL particles for the luminescence pixels (see Experimental Section and Figure S7, Supporting Information for details). Figure 4c and Video S2 (Supporting Information) show an orange "DRY" pattern at a low RH, transforming into a green "WET" pattern as the RH exceeded 60%, with the corresponding luminescent spectra and chromaticity diagram showing in the bottom panel of Figure 4c.

Another innovative application of CUISD is the real-time spatial mapping of fingertip moisture, which provides a strategy for fingertip motion tracking for contactless human–machine interactions (HMIs). Figure 4d shows a high-resolution CUISD with 7569 pixels arranged in an area of 3.4 × 3.4 cm^2, in which the pixels with a size of 200 µm × 200 µm were only deposited onto the electrodes to avoid the inter-gap luminescence. The shape of the fingertip closed to the high-resolution CUISD was well recognized (Figure 4e, Video S3, Supporting Information), and the 3D intensity profile of the corresponding luminous pixels can be extracted using a self-developed program (Figure 4f). A large-scale (Maximum 10 cm × 10 cm) multicolor CUISD was also developed for motion tracking and discrimination of multifingers, as shown in Figures 4g,h and S8 (Supporting Information), which is more suitable for interaction control. This concept was validated by implementing a contactless user interaction system utilizing CUISD. This system, as illustrated in Figure 4i, comprises three units: i) acquisition, where a multicolor CUISD with specific shapes (Figure S9, Supporting Information) transforms fingertip humidity signals into light signals; ii) transmitter, where a camera captures light signals and encodes them through STM32, and the encoded information is transmitted to the cloud via a Wi-Fi module; and iii) receiver, where another Wi-Fi module on the RC car receives signals, generating commands to control the car movement and the robotic arm manipulation through a microcontroller unit (MCU). Utilizing this scheme, color discrimination and trajectory recognition of humidity-induced luminescence signals were identified. As shown in Figure 4j, an orange light was applied to the commands for the robotic arm to pick up and drop down objects, and the trajectory of the green light was assigned to the motion of the trolley. Thus, the precise operation of an RC car to carry objects to the designated locations was demonstrated, as shown in Figure 4k and Video S4 (Supporting Information).

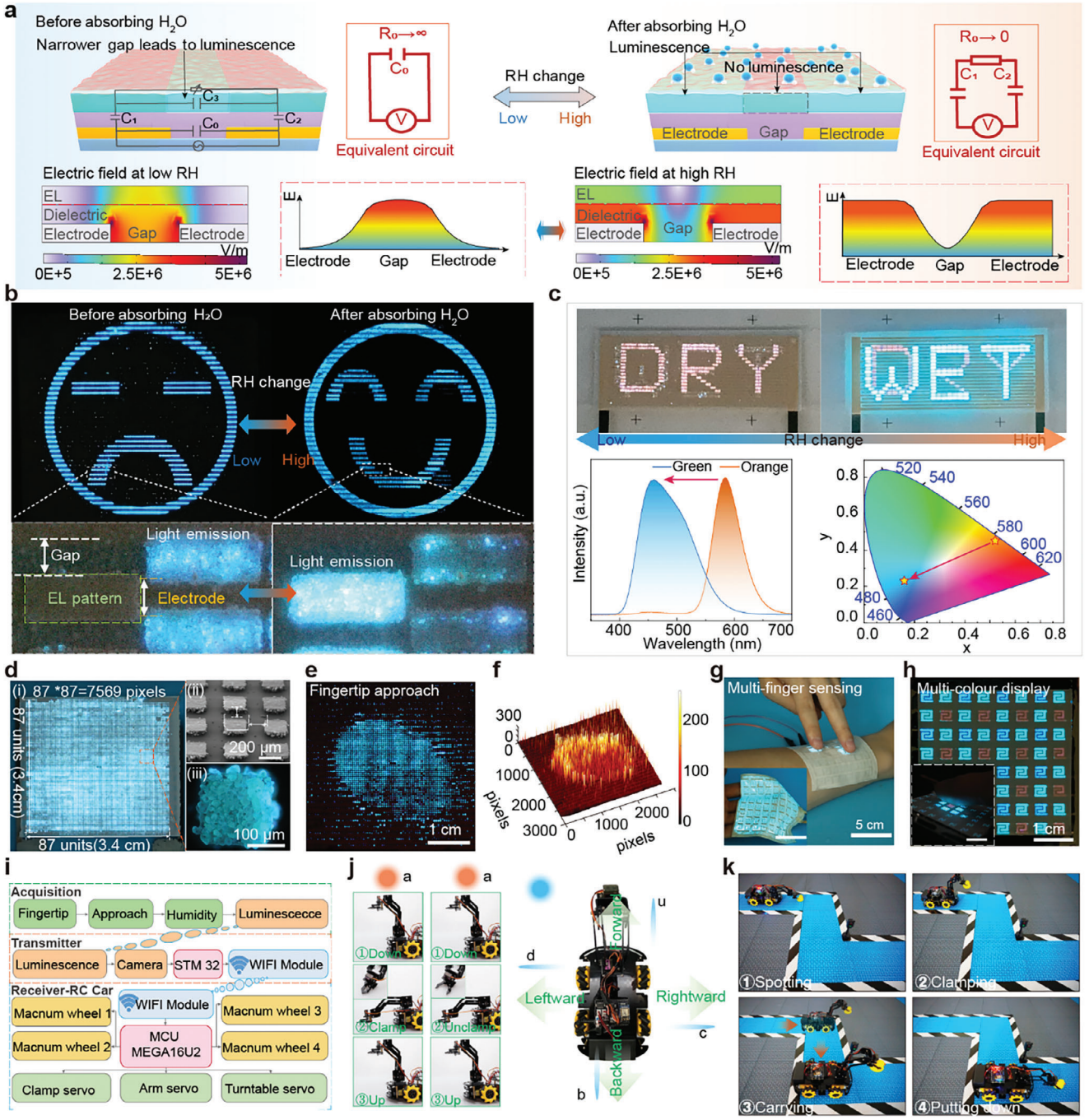

Figure 4. CUISD for dynamic display and motion tracking. a) Schematic of the working mechanism and simulation of the dynamic display of the CUISD. b) Optical images of CUISD with the dynamic transition of images. c) Optical images of CUISD with simultaneous dynamic display and color changes. d) Optical images of a high-resolution CUISD with 7569 pixels arranged in an area of 3.4 × 3.4 cm^2. e) Spatial mapping of fingertip moisture. f) 3D intensity profile of the corresponding luminous pixels. g,h) Large-scale multicolor CUISD for multi-finger sensing. i) Flowchart of the humidity-induced luminescence signal recognition method. j) Logic commands and corresponding actions of the RC car. k) Precise control of an RC car to carry an object using the CUISD.

2.5. CUISD for Breath-Based Interaction Systems

Breathing, an incessant and involuntary biomechanical process, endures throughout an individual's lifespan, irrespective of their psychological or physiological state. For those grappling with profound paralysis or disabilities that result in the loss of physical mobility and language skills, respiration emerges as their sole avenue of communication. Consequently, the development of a breath-triggered interaction interface becomes imperative, facilitating effective communication among individuals with paralysis

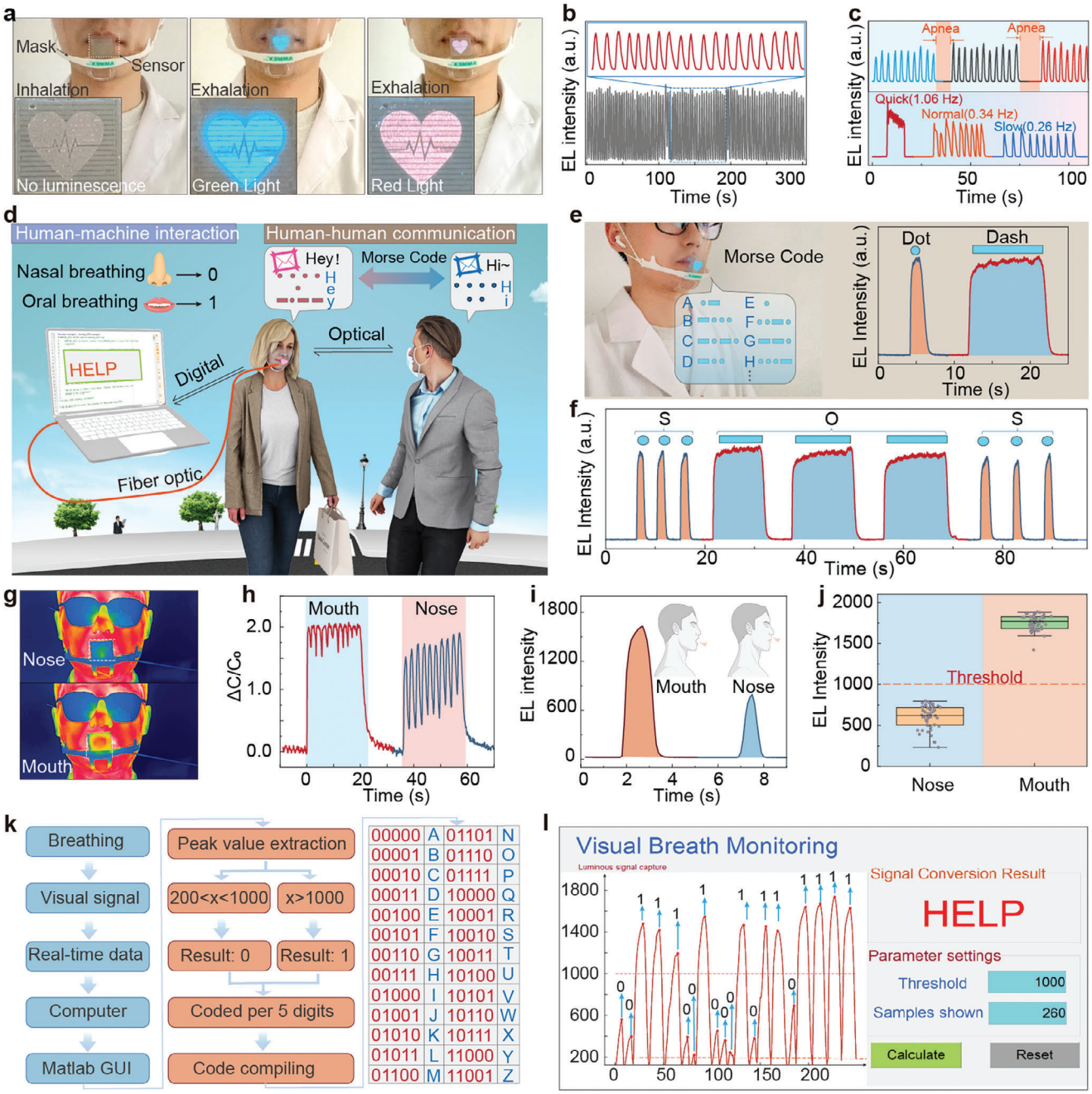

Figure 5. CUISD for breath-based interaction systems. a) Mask integrated with a CUISD for breath-based interactions. b) Luminescence intensity of the CUISD mask under continuous exhalation and inhalation. c) Luminescence response of the CUISD mask under different breathing states. d) Conceptual diagram of the CUISD mask for human–human interaction and human–machine interactions. e,f) Morse codes generated by the CUISD mask for human–human communication. g) Infrared thermograms of the CUISD mask during oral and nasal exhalation. h) Relative capacity change of the CUISD mask during oral and nasal exhalation. i) Luminescence intensity of the CUISD mask during oral and nasal exhalation. j) Statistics of peak luminescence intensity of nasal and oral respiration. The results were obtained by counting the changes in luminescence intensity induced by 50 oral breaths and 50 nasal breaths. k) Flowchart of the human–machine interaction system utilizing the respiratory signals. l) The binary data is achieved by alternating nasal and oral breathing, delivering the information of "HELP" unambiguously.

or disabilities. As depicted in **Figure** 5a, the CUISD was seamlessly integrated into a mask to transform breath into luminescent signals, offering customizable display options through easily adjustable colors. Real-time monitoring of luminescence intensity revealed the fluctuating patterns, mirroring dynamic respiration (Figure 5b). During exhalation, the water molecules in the exhaled gas decreased the resistance of the sensing layer and enhanced the luminescence. Meanwhile, during inhalation, the desorption of water molecules increased the resistance, leading to attenuated luminescence intensity. Additionally, the CUISD

mask performed effectively even after the wearer consumed water or alcohol. As shown in Figure S10 (Supporting Information), water or alcohol intake increased the luminescence intensity owing to the increased amount of water molecules in the exhaled gas. Notably, the recovery time for luminescence was shorter after alcohol consumption than that after water consumption owing to the superior volatility of alcohol. These response features showcase the suitability of the CUISD mask for interaction applications. Also, this introduce new possibilities in healthcare. As shown in Figure 5c, the apnea halted luminescence, and changes in respiratory rate were manifested in luminescence frequencies.

The applications of the CUISD mask in both human–human and human–machine interactions are illustrated in Figure 5d. The Morse code, an established method of information transmission, was used to decipher the luminescence signals induced by breathing from the CUISD mask to enable real-time communication. Figure 5e shows the dot represented by the flashing luminescence produced by a short breath and the dash represented by the continuous luminescence produced by a long breath. Encoding luminescence based on different exhalation durations enabled the transmission of an "SOS" message (Figure 5f). Consequently, breath control facilitates the transmission of luminescent signals encoded by the Morse code, enabling intuitive visual human–human interaction. Furthermore, we developed a human–machine interaction system for acquiring and analyzing respiratory signals. As shown in Figure 5g, the temperature changes in the CUISD mask from the exhalation through the nose and mouth exhibited significant variations because of the smaller volume of air exhaled through the nose and larger distance from the CUISD compared to the mouth. This conclusion was confirmed by the capacitance changes induced by nose and mouth breathing, as shown in Figure 5h. Figure 5i demonstrated the disparity in the luminescence intensity induced by nose and mouth exhalation, whereby mouth breathing elicited a more intense luminescence. The statistical analysis of the luminescence intensity of 50 breaths from the nose and the mouth further indicated that mouth breathing resulted in a substantially larger luminous intensity than nose breathing (Figure 5j). The information conversion process involves assigning a value of "0" or "1" to the luminous intensity caused by nose and mouth breathing using a translation program with a specified threshold (threshold = 1000). The signal conversion process is detailed in Figure 5k, wherein the luminescence induced by nose and mouth breathing was converted into real-time data by the spectrometer and transmitted to the computer and then displayed as letters using the MATLAB program. The MATLAB program determined peaks by assigning a value of "0" if the peak intensity is between 200–1000 and "1" if the peak intensity exceeded 1000, encoding every five values into a letter via a binary cipher. Figure 5l and Video S5 (Supporting Information) show the binary data achieved by alternating nasal and oral breathing, where the delivered information of "HELP" can be recognized unambiguously.

3. Conclusion

We demonstrated a single-device CUISD with attributes of stretchability, large-area, high-resolution, fast-response, multicolor, and dynamic visualization for contactless interaction applications. The CUISD relied on the ACEL triggered by humidity as a fingertip approached or with respiration. The control of an RC car to carry objects to a designated location through contactless finger movements was demonstrated using CUISD to visualize finger proximity and accurately track its position. A smart mask integrated with a CUISD was realized, exhibiting the unique capability of recognizing breathing patterns for human–human and human–machine interactions, which is important for the communication of individuals with physical and sensory impairments. The present findings provide a supplementary channel for current interaction technologies, holding immeasurable application prospects in the fields of virtual/augmented reality and metaverses.

4. Experimental Section

Materials: PDMS (SYLGARD 184, Dow Corning), polyvinyl alcohol (PVA) powder (molecular weight, 80000), $BaTiO_3$ (99.9%, Aladdin), ZnS: Cu and ZnS: Mn (Shanghai Keyan Phosphor Technology Co., Ltd.), a negative photoresist (NR9-3000PY, FUTURREX), a negative tone photo-epoxy (SU-8 GM-1070, GERSTELTEC), a moisture-absorbing hydrogel (Shanghai Mifang Electronic Technology Co., Ltd.), and HNO_3 (5 M, Sigma-Aldrich) were used as received in this study.

Preparation of the Multilayer Ag NF Electrodes: A 10 wt.% polyvinyl alcohol (PVA) aqueous solution was prepared by mixing PVA powder (molecular weight: 80 000) with deionized water. The mixture was stirred at 1000 rpm for 24 h at 60 °C to obtain a homogeneous solution. Randomly oriented PVA nanofibers were then electrostatically spun onto circular metal frames (8 cm diameter conductive ring) using a Shenzhen Tongli Technology Co., Ltd. setup. The PVA solution was injected through a G7 needle via a syringe pump at 0.3 mL h^{-1}, with a constant voltage of 11 kV applied between the needle and the grounded substrate (8 cm diameter conductive ring). A layer of Ag (≈150 nm) was coated on the nanofibers using magnetron sputtering, resulting in PVA/Ag core–shell structured nanofibers. The Ag/PVA was transferred to a deionized water surface, picked up with glass, and then patterned using negative photoresist through photolithographic steps. After etching and cleaning, a layer of PDMS (20:1 ratio) was spin-coated, cured, and peeled off, yielding the PDMS-embedded Ag nanofibers electrode.

Fabrication of the CUISD: The fabricated Ag NFs electrodes were treated with plasma, and then a dielectric layer with a $BaTiO_3$ to PDMS mass ratio of 1:1 was spin-coated on top of the electrodes at 3000 rpm for 60 s. The electrodes were dried and then coated with ZnS: Cu and PDMS at a mass ratio of 2:1. For the stretchable CUISD, the luminescent layer was obtained by spin-coating ZnS: Cu with PDMS at a mass ratio of 2:1 at 3000 rpm for 60 s. For the dynamic displays and high-resolution CUISDs, the luminescent layer was achieved by mixing ZnS: Cu with a negative-tone photo-epoxy (SU-8 GM-1070) at a mass ratio of 2:1 through a series of photolithographic processes The multicolor display was achieved by the two-step alignment photolithography of ZnS: Cu and ZnS: Mn mixed with photo-epoxy. After curing the luminescent layer, the moisture-absorbing hydrogel of the sensing layer was scraped onto the surface of the luminescent layer and dried using a nitrogen gas gun.

Signal Recognition and Interaction of the CUISD: The recognition of the light-emitting color and the direction of the luminescence trajectory of the device were based on a set of embedded systems, containing an ESP8266 Wi-Fi module, an OV5640 camera module, a liquid crystal display (LCD) display with a resolution of 800 × 480, and an STM32F767 core processor. The optical signal of the device was captured by the OV5640 camera module, and the MCU displayed the captured data stream to the LCD, and then extracted the RGB coordinates of the optical signal from the LCD, and compared the RGB coordinates with the green coordinates RGB = ($0 \le r < 2$, $3 < b \le 5$, $2 < g \le 5$) and the orange coordinates RGB = ($3 < r \le 5$, $0 \le b < 4$, $1 < g \le 5$) that was set up in the MCU in

advance. When the extracted RGB coordinates and the preset orange coordinates were compared successfully, the corresponding command ("a") would be issued directly, and when it was compared successfully with the preset green coordinates, the direction of the light trajectory would be recognized, and the corresponding commands would be issued after recognizing the different directions (up, down, left, and right corresponding to "u", "b", "d", and "c", respectively). The principle of light track recognition was as follows: LCD could be regarded as an 800 × 480 coordinate system, MCU would record the pixel coordinates of green light under different frames and obtained the direction of the light track by comparing the coordinates of the green light under different frames.

The RC car could be divided into four core parts: The Arduino UNO core board for the master control, an ESP8266 module for receiving signals, a clamp composed of clamp/arm/tunable servo motors, and wheels for controlling the movement. When the car received the command "a" for the first time, the Arduino marked state 1 for the clamping operation, and when it received "a" for the second time, the Arduino marks state 2 for the return operation. When the car received the "u", "b", "d", "c" signals, it moved forward, backward, to the left, and to the right, respectively.

Characterizations: The SEM (FEI Nova NanoSEM 450) equipped with EDAX was employed to characterize morphology and composition. XRD patterns were obtained using a PANalytical X'Pert 3 Powder diffractometer with Cu Kα radiation. Surface roughness and electrical conductivity were measured via AFM (Asylum Research MFP-3D-SA). Total reflectance FT-IR spectra were obtained using a VERTEX80v spectrophotometer. Transmission spectra were detected by a UV–vis–NIR spectrophotometer (Shimadzu UV 3600). Permittivity was measured with a Nanocontral Concept 90 dielectric impedance spectrometer. Resistance and capacitance were recorded with an Agilent E4980A LCR meter. Square resistance was characterized using a four-point probe meter (Xinyangdianzi CXT-2663). Mechanical properties and stability were tested with a Yuelian YL-S71 tensile machine and LinMot E1100 linear motor, respectively. Relative humidity was measured with a HABOTEST-HT618 humidity meter. Humidity-induced luminescence properties were assessed using a fiber optic spectrometer (Ocean QE65 Pro) and a screen luminance meter (Xinbao-SM208) in a constant temperature and humidity test chamber (Aerospace Zhida Test Equipment Co., Ltd. Y HD-150 L).

Statistical Analysis: The diameter statistics in Figure 2f were obtained by counting randomly selected SEM images of Ag NFs electrodes by Image J software. The error bars in Figure 2h were based on three independent measurements of three devices and the results were expressed as standard deviations. Figure 5j was obtained by taking the results of 50 oral breaths and 50 nasal breaths respectively and performing discrete statistics in the Origin software.

Supporting Information

Supporting Information is available from the Wiley Online Library or from the author.

Acknowledgements

The authors thank the support of National Natural Science Foundation of China (No. 52125205, 52250398, U20A20166, 52192614, 52003101, 52372154, U22A2077, and 52002246), National key R&D program of China (2021YFB3200300), Natural Science Foundation of Beijing Municipality (2222088), Shenzhen Science and Technology Program (Grant No. KQTD20170810105439418), Shenzhen High-End Talent Scientific Research Program and the Fundamental Research Funds for the Central Universities.

Conflict of Interest

The authors declare no conflict of interest.

Data Availability Statement

The data that support the findings of this study are available from the corresponding author upon reasonable request.

Keywords

breathing monitoring, contactless sensing, human–machine interactions, user-interactive sensing displays, visual humidity sensing

Received: February 5, 2024
Revised: March 18, 2024
Published online:

[1] C. Lai, S. Tanaka, T. D. Harris, A. K. Lee, *Science* **2023**, *382*, 566.
[2] D. Ahn, J. Yang, M. Cha, H. Yang, J. Kim, S. Park, S. Han, E. Lee, S. Lee, S. Park, *Nat. Commun.* **2023**, *14*, 6811.
[3] Y. Huang, J. Zhou, P. Ke, X. Guo, C. K. Yiu, K. Yao, S. Cai, D. Li, Y. Zhou, J. Li, T. H. Wong, Y. Liu, L. Li, Y. Gao, X. Huang, H. Li, J. Li, B. Zhang, Z. Chen, H. Zheng, X. Yang, H. Gao, Z. Zhao, X. Guo, E. Song, H. Wu, Z. Wang, Z. Xie, K. Zhu, X. Yu, *Nat. Electron.* **2023**, *6*, 1041.
[4] L. Wang, N. Li, Y. Zhang, P. Di, M. Li, M. Lu, K. Liu, Z. Li, J. Ren, L. Zhang, P. Wan, *Matter* **2022**, *5*, 3417.
[5] Y. Roh, S. Lee, S. M. Won, S. Hwang, D. Gong, C. Kim, I. Hong, D. Lim, H. Kim, M. Kim, B. Kim, T. Kim, S. Im, D. Shin, U. Kim, J. Choi, J.-S. Koh, D. Kang, S. Han, *Nat. Electron.* **2024**, *7*, 66.
[6] S. Yu, T. H. Park, W. Jiang, S. W. Lee, E. H. Kim, S. Lee, J.-E. Park, C. Park, *Adv. Mater.* **2023**, *35*, 2204964.
[7] W. Jiang, S. Lee, G. Zan, K. Zhao, C. Park, *Adv. Mater.* **2024**, *36*, 2304053.
[8] X. Ma, C. Wang, R. Wei, J. He, J. Li, X. Liu, F. Huang, S. Ge, J. Tao, Z. Yuan, P. Chen, D. Peng, C. Pan, *ACS Nano* **2022**, *16*, 2789.
[9] C. Wang, D. Hwang, Z. Yu, K. Takei, J. Park, T. Chen, B. Ma, A. Javey, *Nat. Mater.* **2013**, *12*, 899.
[10] C. Pan, L. Dong, G. Zhu, S. Niu, R. Yu, Q. Yang, Y. Liu, Z. L. Wang, *Nat. Photonics* **2013**, *7*, 752.
[11] J. I. Lee, H. Choi, S. H. Kong, S. Park, D. Park, J. S. Kim, S. H. Kwon, J. Kim, S. H. Choi, S. G. Lee, D. H. Kim, M. S. Kang, *Adv. Mater.* **2021**, *33*, 2100321.
[12] B. Lee, J.-Y. Oh, H. Cho, C. W. Joo, H. Yoon, S. Jeong, E. Oh, J. Byun, H. Kim, S. Lee, J. Seo, C. W. Park, S. Choi, N.-M. Park, S.-Y. Kang, C.-S. Hwang, S.-D. Ahn, J.-I. Lee, Y. Hong, *Nat. Commun.* **2020**, *11*, 663.
[13] Y. Guo, H. Li, Y. Li, X. Wei, S. Gao, W. Yue, C. Zhang, F. Yin, S. Zhao, N.-Y. Kim, G. Shen, *Adv. Funct. Mater.* **2022**, *32*, 2203585.
[14] Y.-J. Quan, Y.-G. Kim, M.-S. Kim, S.-H. Min, S.-H. Ahn, *ACS Nano* **2020**, *14*, 5392.
[15] J. Sendra, F. Haake, M. Calvo, H. Galinski, R. Spolenak, *Adv. Funct. Mater.* **2023**, *33*, 2302179.
[16] J. Ma, Y. Yang, C. Valenzuela, X. Zhang, L. Wang, W. Feng, *Angew. Chem., Int. Ed.* **2022**, *61*, e202116219.
[17] C. Li, N. Schramma, Z. Wang, N. F. Qari, M. Jalaal, M. I. Latz, S. Cai, *Sci. Adv.* **2023**, *9*, eadi8643.
[18] C. Wang, H. Hu, D. Peng, L. Dong, D. Z, *Soft Sci.* **2023**, *3*, 39.
[19] J. He, R. Wei, S. Ge, W. Wu, J. Guo, J. Tao, R. Wang, C. Wang, C. Pan, *InfoMat* **2023**, *6*, e12493.
[20] R. Wei, J. He, S. Ge, H. Liu, X. Ma, J. Tao, X. Cui, X. Mo, Z. Li, C. Wang, C. Pan, *Adv Mater* **2023**, *8*, 2200757.
[21] C. Wang, R. Ma, D. Peng, X. Liu, J. Li, B. Jin, A. Shan, Y. Fu, L. Dong, W. Gao, Z. L. Wang, C. Pan, *InfoMat* **2021**, *3*, 1272.
[22] C. Ge, X. An, X. He, Z. Duan, J. Chen, P. Hu, J. Zhao, Z. Wang, J. Zhang, *Adv. Sci.* **2023**, *10*, 2301341.
[23] W. Liu, F. Xiang, D. Mei, Y. Wang, *Adv Mater* **2024**, *9*, 2301685.

[24] Y. Lu, G. Yang, Y. Shen, H. Yang, K. Xu, *Nano-Micro Lett.* **2022**, *14*, 150.
[25] S. Li, Y. Wu, W. Asghar, F. Li, Y. Zhang, Z. He, J. Liu, Y. Wang, M. Liao, J. Shang, L. Ren, Y. Du, D. Makarov, Y. Liu, R.-W. Li, *Adv. Sci.* **2023**, 2304525.
[26] P. Makushko, E. S. Oliveros Mata, G. S. Cañón Bermúdez, M. Hassan, S. Laureti, C. Rinaldi, F. Fagiani, G. Barucca, N. Schmidt, Y. Zabila, T. Kosub, R. Illing, O. Volkov, I. Vladymyrskyi, J. Fassbender, M. Albrecht, G. Varvaro, D. Makarov, *Adv. Funct. Mater.* **2021**, *31*, 2101089.
[27] X. Guo, X. Lu, P. Jiang, X. Bao, *Adv. Mater.* **2022**, *34*, 2204355.
[28] H. L. Wang, Y. Wang, *ACS Nano* **2023**, *17*, 20723.
[29] H. Zhou, W. Huang, Z. Xiao, S. Zhang, W. Li, J. Hu, T. Feng, J. Wu, P. Zhu, Y. Mao, *Adv. Funct. Mater.* **2022**, *32*, 2208271.
[30] K. Shrestha, S. Sharma, G. B. Pradhan, T. Bhatta, P. Maharjan, S. S. Rana, S. Lee, S. Seonu, Y. Shin, J. Y. Park, *Adv. Funct. Mater.* **2022**, *32*, 2113005.
[31] N. Dai, X. Guan, C. Lu, K. Zhang, S. Xu, I. M. Lei, G. Li, Q. Zhong, P. Fang, J. Zhong, *ACS Nano* **2023**, *17*, 24814.
[32] W. Liu, Y. Duo, J. Liu, F. Yuan, L. Li, L. Li, G. Wang, B. Chen, S. Wang, H. Yang, Y. Liu, Y. Mo, Y. Wang, B. Fang, F. Sun, X. Ding, C. Zhang, L. Wen, *Nat. Commun.* **2022**, *13*, 5030.
[33] T. Kamijo, A. J. J. M. van Breemen, X. Ma, S. Shanmugam, T. Bel, G. de Haas, B. Peeters, R. Petre, D. Tordera, R. Verbeek, H. B. Akkerman, L. M. Hagelsieb, F. de Roose, I. Lieberman, F. Yamaguchi, R. A. J. Janssen, E. A. Meulenkamp, A. J. Kronemeijer, G. H. Gelinck, *Nat. Electron.* **2023**, *6*, 451.
[34] S. W. Lee, S. Baek, S.-W. Park, M. Koo, E. H. Kim, S. Lee, W. Jin, H. Kang, C. Park, G. Kim, H. Shin, W. Shim, S. Yang, J.-H. Ahn, C. Park, *Nat. Commun.* **2020**, *11*, 6072.
[35] H. S. Kang, S. W. Han, C. Park, S. W. Lee, H. Eoh, J. Baek, D.-G. Shin, T. H. Park, J. Huh, H. Lee, D.-E. Kim, D. Y. Ryu, E. L. Thomas, W.-G. Koh, C. Park, *Sci. Adv.* **2020**, *6*, eabb5769.
[36] S. An, H. Zhu, C. Guo, B. Fu, C. Song, P. Tao, W. Shang, T. Deng, *Nat. Commun.* **2022**, *13*, 1446.